6. A. N. Vamivakas *et al.*, *Nano Lett.* **7**, 2892 (2007).
7. A. Muller *et al.*, *Phys. Rev. Lett.* **99**, 187402 (2007).
8. J. T. Shen, S. Fan, *Phys. Rev. Lett.* **95**, 213001 (2005).
9. D. E. Chang, A. S. Sorensen, E. A. Demler, M. D. Lukin, *Nat. Phys.* **3**, 807 (2005).
10. J. M. Raimond, M. Brune, S. Haroche, *Rev. Mod. Phys.* **73**, 565 (2001).
11. A. Wallraff *et al.*, *Nature* **431**, 162 (2004).
12. D. I. Schuster *et al.*, *Nature* **445**, 515 (2007).
13. A. Fragner *et al.*, *Science* **322**, 1357 (2008).
14. L. S. Bishop *et al.*, *Nat. Phys.* **5**, 105 (2009).
15. M. Baur *et al.*, *Phys. Rev. Lett.* **102**, 243602 (2009).
16. A. A. Houck *et al.*, *Nature* **449**, 328 (2007).
17. O. Astafiev *et al.*, *Nature* **449**, 588 (2007).
18. M. Hofheinz *et al.*, *Nature* **459**, 546 (2009).
19. S. G. Rautian, I. I. Sobel'man, *Sov. Phys. JETP* **14**, 328 (1962).
20. A. I. Burshtein, *Sov. Phys. JETP* **21**, 567 (1965).
21. B. R. Mollow, *Phys. Rev.* **188**, 1969 (1969).
22. F. Schuda, C. R. Stroud Jr., M. Hercher, *J. Phys. B* **7**, L198 (1974).
23. F. Y. Wu, R. E. Grove, S. Ezekiel, *Phys. Rev. Lett.* **35**, 1426 (1975).
24. J. E. Mooij, T. P. Orlando, L. Levitov, L. Tian, C. H. van der Wal, S. Lloyd, *Science* **285**, 1036 (1999).
25. Materials and methods are available as supporting material on *Science* Online.
26. A. A. Abdumalikov, O. Astafiev, Y. Nakamura, Y. A. Pashkin, J.-S. Tsai, *Phys. Rev. B* **78**, 180502 (2008).
27. R. J. Schoelkopf, A. A. Clerk, S. M. Girvin, K. W. Lehnert, M. H. Devoret, *Quantum Noise in Mesoscopic Physics*, Y. V. Nazarov, ed. (Kluwer Academic Press, Norwell, MA, 2002), pp. 175–203.
28. F. Yoshihara, K. Harrabi, A. O. Niskanen, Y. Nakamura, J. S. Tsai, *Phys. Rev. Lett.* **97**, 167001 (2006).
29. A. L. Rakhmanov, A. M. Zagoskin, S. Savel'ev, F. Nori, *Phys. Rev. B* **77**, 144507 (2008).

30. This work was supported by the Core Research for Evolutional Science and Technology, Japan Science and Technology Agency and the Ministry of Education, Culture, Sports, Science and Technology kakenhi "Quantum Cybernetics."

Supporting Online Material

www.sciencemag.org/cgi/content/full/327/5967/840/DC1
Materials and Methods
Fig. S1

14 September 2009; accepted 15 December 2009
10.1126/science.1181918

Spin-Dependent Quantum Interference Within a Single Magnetic Nanostructure

H. Oka, P. A. Ignatiev, S. Wedekind, G. Rodary,* L. Niebergall, V. S. Stepanyuk,† D. Sander,† J. Kirschner

Quantum interference is a coherent quantum phenomenon that takes place in confined geometries. Using spin-polarized scanning tunneling microscopy, we found that quantum interference of electrons causes spatial modulation of spin polarization within a single magnetic nanostructure. We observed changes in both the sign and magnitude of the spin polarization on a subnanometer scale. A comparison of our experimental results with ab initio calculations shows that at a given energy, the modulation of the spin polarization can be ascribed to the difference between the spatially modulated local density of states of the majority spin and the nonmodulated minority spin contribution.

When electrons are confined to nanostructures, their dual wave-particle nature comes into full view in experiment. In particular, spatially modulated variations of the electronic local density of states (LDOS) have been observed by scanning tunneling microscopy (STM) (*1*, *2*). These modulation patterns reflect quantum interference between electron waves that are scattered off the boundaries of a nanostructure, forming a standing wave.

In addition to charge, electrons also carry a spin. When confined to magnetic nanostructures, an imbalance between electrons of opposite spin orientations leads to spin-polarized electron waves, giving rise to spin-dependent quantum interference. Recent theoretical studies predicted that local spin polarization on nonmagnetic surfaces as well as on magnetic nanostructures can be spatially modulated (*3*–*5*).

We observed spin-dependent quantum interference by means of spin-polarized STM (SP-STM) (*6*), a technique sensitive to surface magnetization. The nanostructures we study are triangular Co islands located on a nonmagnetic substrate, the (111) surface of copper (*4*, *7*–*10*). A previous study, which investigated a system similar to ours but under different conditions, indicated the dependence of electron confinement on the spin character of electronic states (*9*).

The SP-STM measurements were performed at a temperature of 8 K. To detect magnetic contrast, we used W tips covered with magnetic materials (Cr-Co-W tips) and external magnetic fields up to $B = 4$ T. To explore the spatial distribution of the spin polarization, we measure the spatially resolved map of the differential tunneling conductance (dI/dV) asymmetry, $A_{dI/dV}$, defined by

$$A_{dI/dV} \equiv \frac{dI/dV_{AP} - dI/dV_P}{dI/dV_{AP} + dI/dV_P} \qquad (1)$$

where dI/dV_{AP} and dI/dV_P are the dI/dV signals measured with the tip and sample magnetization in antiparallel (AP) and parallel (P) configurations, respectively. The dI/dV signal depends on the relative orientation of the tip and sample magnetizations, which is described in the generalized Tersoff-Hamann model (*11*, *12*). Using that model, we can link the dI/dV asymmetry $A_{dI/dV}$ to the spin polarization of the tip, P_T, and of the sample at the tip apex position, P_S (*10*, *13*):

$$A_{dI/dV} = -P_T P_S \qquad (2)$$

A constant-current STM image (Fig. 1) shows a typical triangular Co island on Cu(111) (*14*, *15*). To link the dI/dV asymmetry with the spin polarization of the sample, we characterize the magnetization orientation of the Co island with respect to the magnetic tunneling tip. A dI/dV hysteresis loop, in which we plot the dI/dV signal as a function of the magnetic field at a fixed energy, allows us to identify the magnetic configurations (fig. S1) (*16*–*18*).

To extract the $A_{dI/dV}$ maps of the Co island, we recorded two dI/dV images on the exact same island with AP (Fig. 2A) and P (Fig. 2B) magnetization configurations, at a bias voltage of $V = +0.03$ V. Note that it is essential to map the dI/dV signal with P and AP configurations on exactly the same island because the electronic structures of Co islands on Cu(111) strongly depend on the size, stacking, and shape of the island, as well as position within the island (*8*, *9*, *19*).

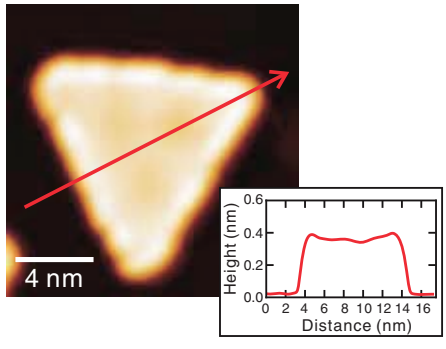

Fig. 1. Constant-current STM image of a triangular Co island on Cu(111); $V_S = -0.1$ V, $I = 1.0$ nA, where V_S is the sample bias voltage with respect to the tip and I is the tunneling current. The inset shows a line profile along the red arrow in the STM image. The Co island is two atomic layers (~0.4 nm) in height and has a base length of 12 nm.

Max-Planck-Institut für Mikrostrukturphysik, Weinberg 2, D-06120 Halle/Saale, Germany.

*Present address: Laboratoire de Photonique et de Nanostructures, CNRS UPR20, Route de Nozay, 91460 Marcoussis, France.

†To whom correspondence should be addressed. E-mail: stepanyu@mpi-halle.de (V.S.S.); sander@mpi-halle.de (D.S.)

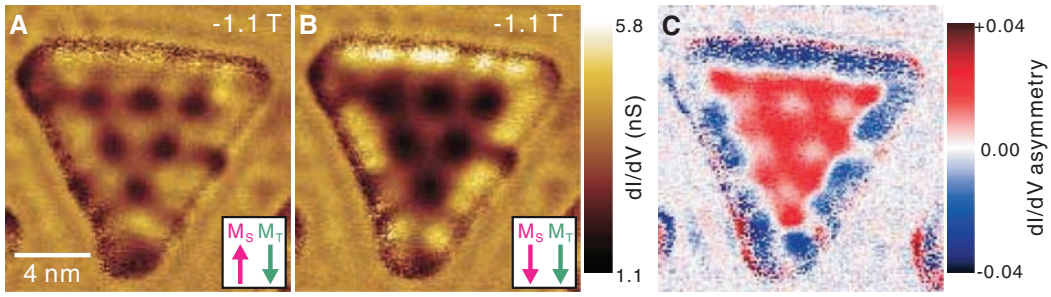

Fig. 2. (**A** and **B**) Two *dI/dV* images of the Co island in Fig. 1, the basis for the *dI/dV* asymmetry map in (C). Both images were recorded at $B = -1.1$ T, but with different magnetization configurations between the magnetic tunneling tip and the Co island: antiparallel (A) and parallel (B). The insets represent the antiparallel (AP) and parallel (P) configurations. $V = +0.03$ V, $V_{stab} = +0.5$ V, and $I = 1.0$ nA, where V is the bias voltage at which the *dI/dV* signal is recorded and V_{stab} is the bias voltage to stabilize the tip before the feedback loop is opened (*10*). (**C**) *dI/dV* asymmetry map calculated using Eq. 1 from the images in (A) and (B).

We used Eq. 1 to calculate the *dI/dV* asymmetry map (Fig. 2C) from the two *dI/dV* images. The *dI/dV* asymmetry near the Fermi level at $V = +0.03$ V is strongly position-dependent within the Co island. At the edge of the island it is negative, whereas the inner part of the island shows largely positive values. This result can be explained by the existence of a rim state, which is localized spatially around the edges of the Co island and energetically around the Fermi level (*9*). The rim state originates from a minority d state (*9*), whereas the inner part of the island mainly has the opposite spin character around the Fermi level and is of majority s-p surface state (*4*, *7*). The magnetization of the tip did not change direction, and the applied bias voltage was fixed at $V = +0.03$ V during the two measurements of the *dI/dV* image. Thus, we can assume that the spin polarization of the tip, P_T, is constant and the *dI/dV* asymmetry is proportional to the spin polarization of the sample—that is, $A_{dI/dV} \propto P_S$. Consequently, we conclude that the inner part of the Co island exhibits a positive *dI/dV* asymmetry because the electronic state with the majority spin character is dominant, and that the edge of the Co island exhibits a negative *dI/dV* asymmetry because the electronic state with the minority spin character is dominant. To interpret the spatial modulation in the *dI/dV* asymmetry (Fig. 2C), which is not due to the atomic structure of the Co island, we focus our discussion on the inner part of the island and analyze the system theoretically.

Our analysis uses density functional theory implemented in the multiple-scattering Korringa-Kohn-Rostoker Green's function method (*10*, *20*) to calculate spatially resolved maps of the LDOS above a triangular two-atomic-layer Co island on Cu(111) for the majority (Fig. 3A) and minority (Fig. 3B) spins at the Fermi level. The LDOSs for the majority spins are spatially modulated inside the triangular Co island. We ascribe this to a standing wave induced by the electronic confinement of the free electron–like surface state. Minority spins have a constant LDOS, consistent with the understanding that they are mainly due to energetically and spatially localized d states, which are hardly influenced by the electronic confinement (*4*). We extract the spatial distribution of the spin polarization above the Co island, P_{Co} (Fig. 3C), from the two calculated LDOS maps as

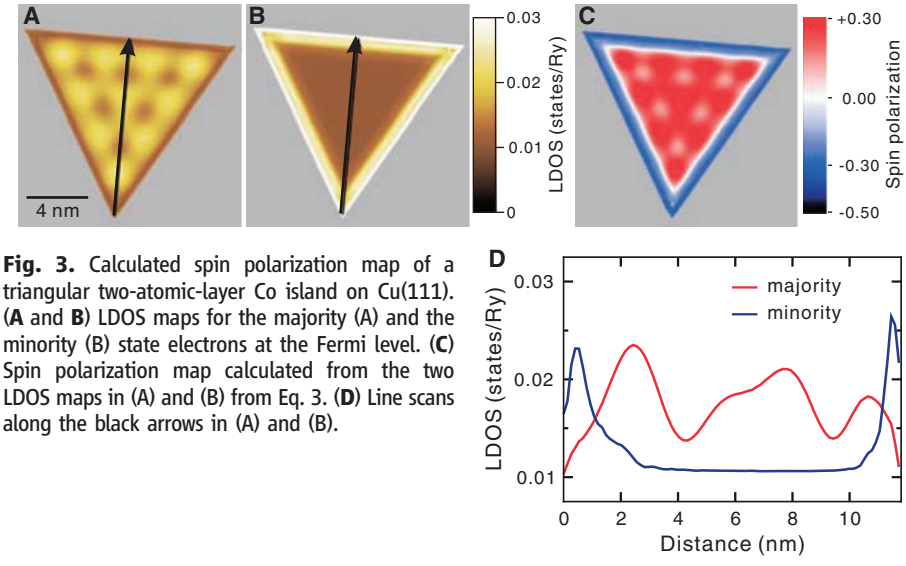

Fig. 3. Calculated spin polarization map of a triangular two-atomic-layer Co island on Cu(111). (**A** and **B**) LDOS maps for the majority (A) and the minority (B) state electrons at the Fermi level. (**C**) Spin polarization map calculated from the two LDOS maps in (A) and (B) from Eq. 3. (**D**) Line scans along the black arrows in (A) and (B).

$$P_{Co} = \frac{n_\uparrow - n_\downarrow}{n_\uparrow + n_\downarrow} \quad (3)$$

where $n_\uparrow$ and $n_\downarrow$ are the LDOS in the vacuum region above the Co island for the majority and minority spins, respectively (*13*). To identify the origin of the largely positive spin polarization observed in Fig. 3C, we present two line profiles (Fig. 3D) of the LDOS maps of Fig. 3, A and B. At the Fermi level, the spatially modulated LDOS of the majority spin is larger everywhere in the inner part of the island than the spatially flat LDOS of the minority spin. This leads to a positive spin polarization, $P_{Co} > 0$ in Eq. 3, in this region.

Comparing Figs. 2C and 3C, we find good agreement between the measured *dI/dV* asymmetry map and the calculated spin polarization map within the inner part of the Co island. Therefore, the *dI/dV* asymmetry map of the Co island can be interpreted as follows: (i) The *dI/dV* asymmetry map qualitatively shows a spatial distribution of the spin polarization on the Co island at a certain energy (figs. S2 and S3) (*21*). (ii) The modulation pattern observed in the *dI/dV* asymmetry map mainly originates from that in the LDOS of the majority spin, which is ascribed to the electron quantum confinement of the free electron–like s-p surface state. Thus, the spin polarization within the Co island is spatially modulated because of spin-dependent quantum interference.

Next, we examine the energy dependence of the *dI/dV* asymmetry maps of the same Co island to ensure the interpretation (ii) described above. The modulation pattern in the *dI/dV* asymmetry maps should change with electron energy. The *dI/dV* asymmetry maps (Fig. 4, B to E) show clear spatial modulations, similar to those in the corresponding *dI/dV* images (fig. S4), with modulation patterns strongly dependent on energy. This is easily understood by considering the origin of the modulation pattern, which is electron confinement of the free electron–like s-p surface state. The s-p surface state starts around −0.2 eV below the Fermi level and exhibits a parabolic dispersion with a positive effective mass (*7*, *9*). With increasing energy, the parallel wave vector ($k_{||}$) of the s-p surface state increases; that is, the wavelength (λ) of the standing waves becomes shorter. The modulation pattern observed in the *dI/dV* asymmetry maps shows the same trend as the standing wave pattern in the *dI/dV* images. This result corroborates the interpretation (ii) of the *dI/dV*

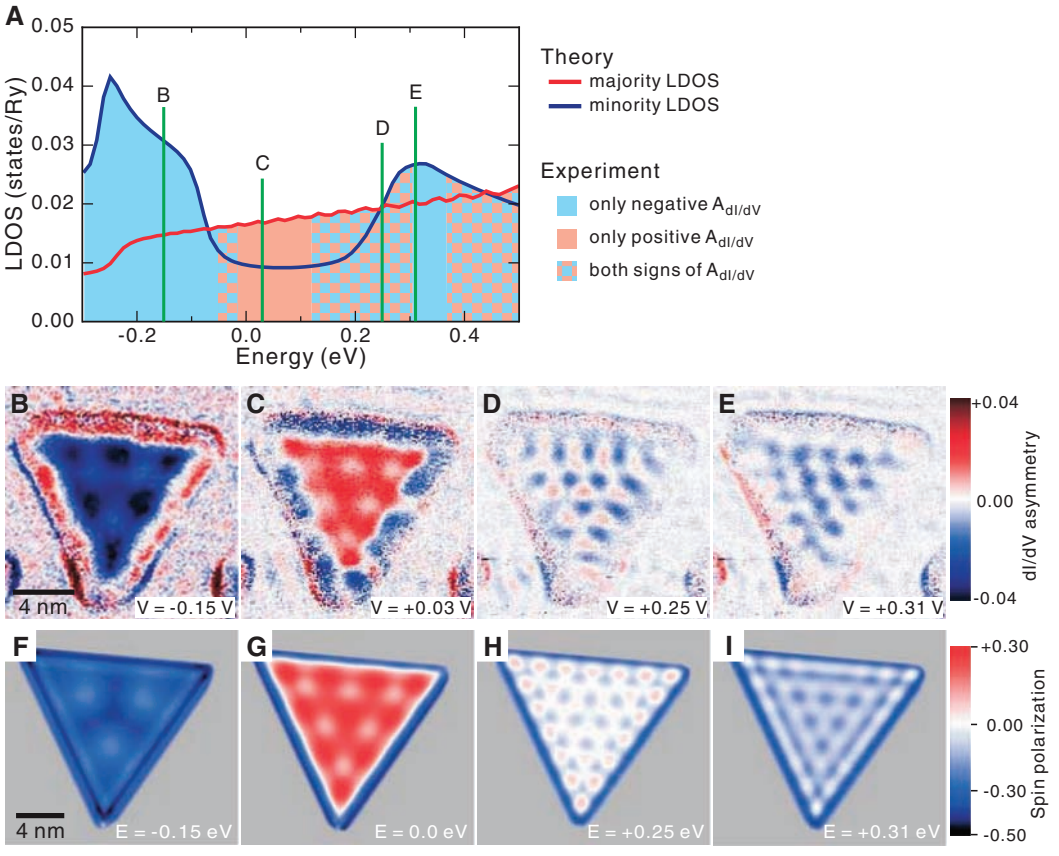

Fig. 4. Energy dependences of the measured *dI/dV* asymmetry maps and calculated spin polarization maps of the Co islands. (**A**) Calculated spin-resolved LDOS of a two-atomic-layer Co film on Cu(111). (**B** to **E**) Experimental *dI/dV* asymmetry maps measured on the Co island of Fig. 1. The *dI/dV* asymmetry maps are calculated from two *dI/dV* images measured at AP and P states from Eq. 1. Measurement conditions of *dI/dV* images: $B = -1.1$ T, $V_{stab} = +0.5$ V, $I = 1.0$ nA. (**F** to **I**) Calculated spin polarization maps of the triangular Co island. The spatial dependence of the spin polarization as defined by Eq. 3 is shown by the maps, which are calculated from two LDOS maps for the majority and the minority states. Vertical green lines in (A) correspond to the energy positions where the *dI/dV* asymmetry maps are obtained. A color map in (A) indicates the energy area where experimental results for the inner part of the Co island show only positive (blue), only negative (red), or both signs (lattice pattern with blue and red) of the *dI/dV* asymmetry in the *dI/dV* asymmetry maps.

asymmetry maps. Unexpectedly, we also find in Fig. 4, B to E, that the sign of the *dI/dV* asymmetry changes with respect to energy, whereas the map at $V = +0.25$ V (Fig. 4D) reveals oscillatory change of the sign as a function of position.

To explore the physics behind these surprising results, we plotted a calculated spin-resolved LDOS above a bilayer Co film on Cu(111) as a function of energy (Fig. 4A). Here we focus on the energy range where the free electron–like s-p surface state arises. The LDOS for the majority spin monotonically increases from $E = -0.25$ eV with increasing energy, which is ascribed to the free electron–like s-p surface state. In contrast, the LDOS for the minority spin shows two energetically localized d states around $E = -0.25$ eV and +0.30 eV, and it is featureless in the interval between them. The spin-resolved LDOS plots reveal that the dominant spin character strongly depends on energy. We can never conclude that the majority spin character is dominant, even in the energy range where the standing wave pattern, which results from the majority s-p surface state, is clearly observed. We must precisely take into account the dominant spin character at a given energy as revealed by the calculations to evaluate the spatial distribution of the *dI/dV* asymmetry within the Co island.

At $V = -0.15$ V (Fig. 4B), the inner part of the Co island has a modulated negative value of the *dI/dV* asymmetry. The spin-resolved LDOS plot (Fig. 4A) shows that the minority spin state is dominant at the corresponding energy, $E = -0.15$ eV, as the localized minority d state exists. Thus, the spatially flat LDOS of the minority spin exceeds the spatially modulated LDOS of the majority spin inside the Co island. This leads to the negative spin polarization inside the island, $P_{Co} < 0$, which comes from a negative numerator in Eq. 3 (i.e., $n_\uparrow - n_\downarrow < 0$), in agreement with the calculated spin polarization map (Fig. 4F). We note that the periodicity of the standing waves in the energy range considered, ≥1.5 nm, is much larger than the distance between neighboring Co atoms, ~0.2 nm.

At $E = +0.25$ eV, where the spin-resolved LDOS plots of the majority and the minority spins cross, we expect that the net spin polarization should be zero within the Co island. The spatial distribution of the LDOS of the majority spin is, however, not flat but modulated. The LDOS of the majority spins is larger than that of the minority at a convexity of the standing wave, and the resulting spin polarization is positive. Correspondingly, the LDOS of the majority spins is smaller than that of the minority at a concavity of the standing wave, and the resulting spin polarization is negative. Where the LDOS of the majority spins is comparable to that of the minority at a node of the standing wave, the resulting spin polarization is zero. Therefore, the spin polarization map shows a spatial modulation and the sign of the spin polarization oscillates as a function of position, depending on the magnitude of the modulated LDOS of the majority spin (Fig. 4H).

We add a color map to Fig. 4A to clarify the energy window where the experimental *dI/dV* asymmetry map exhibits only positive, only negative, or both signs of the *dI/dV* asymmetry within the inner part of the Co island. We find that the dominant spin character at a given energy governs the sign of the *dI/dV* asymmetry and its spatial distribution.

The finding that not only the magnitude but also the sign of the spin polarization is spatially and energetically modulated within a single magnetic nanostructure implies that we can easily change or control local spin polarization on a magnetic nanostructure by changing the energy at a given position, or the position at a given energy.

Our method for extracting the *dI/dV* asymmetry map, which requires that the relative magnetization directions of sample and magnetic tip are experimentally determined by in-field SP-STM, allows us to qualitatively visualize the spin polarization of a single nanostructure on an angstrom scale. Recent ab initio calculations predicted that the spin polarization of surface-state electrons on Cu(111) caused by magnetic adatoms can be enhanced within a Cu corral, and the quantum confinement of surface electrons within corrals or islands can be exploited to tailor the exchange interaction between magnetic adatoms (*3*, *22*). When combined with the capability of the STM to manipulate adatoms and assemble engineered nanostructures (*23*, *24*), our method offers a way

to explore and directly image the exchange interaction and the role of conduction electrons mediating the interaction, such as the Ruderman-Kittel-Kasuya-Yosida interaction.

References and Notes

1. M. F. Crommie, C. P. Lutz, D. M. Eigler, *Science* **262**, 218 (1993).
2. J. Li, W.-D. Schneider, R. Berndt, S. Crampin, *Phys. Rev. Lett.* **80**, 3332 (1998).
3. V. S. Stepanyuk, L. Niebergall, W. Hergert, P. Bruno, *Phys. Rev. Lett.* **94**, 187201 (2005).
4. L. Niebergall, V. S. Stepanyuk, J. Berakdar, P. Bruno, *Phys. Rev. Lett.* **96**, 127204 (2006).
5. L. Niebergall *et al.*, *Phys. Rev. B* **74**, 195436 (2006).
6. M. Bode, *Rep. Prog. Phys.* **66**, 523 (2003).
7. L. Diekhöner *et al.*, *Phys. Rev. Lett.* **90**, 236801 (2003).
8. O. Pietzsch, A. Kubetzka, M. Bode, R. Wiesendanger, *Phys. Rev. Lett.* **92**, 057202 (2004).
9. O. Pietzsch *et al.*, *Phys. Rev. Lett.* **96**, 237203 (2006).
10. See supporting material on *Science* Online.
11. J. Tersoff, D. Hamann, *Phys. Rev. Lett.* **50**, 1998 (1983).
12. D. Wortmann, S. Heinze, Ph. Kurz, G. Bihlmayer, S. Blügel, *Phys. Rev. Lett.* **86**, 4132 (2001).
13. We note that the LDOS in vacuum strongly depends on the distance between the STM tip and the scanned surface (*25*).
14. J. de la Figuera, J. E. Prieto, C. Ocal, R. Miranda, *Phys. Rev. B* **47**, 13043 (1993).
15. N. N. Negulyaev *et al.*, *Phys. Rev. B* **77**, 125437 (2008).
16. F. Meier, L. Zhou, J. Wiebe, R. Wiesendanger, *Science* **320**, 82 (2008).
17. G. Rodary, S. Wedekind, D. Sander, J. Kirschner, *Jpn. J. Appl. Phys.* **47**, 9013 (2008).
18. G. Rodary, S. Wedekind, H. Oka, D. Sander, J. Kirschner, *Appl. Phys. Lett.* **95**, 152513 (2009).
19. M. V. Rastei *et al.*, *Phys. Rev. Lett.* **99**, 246102 (2007).
20. K. Wildberger, V. S. Stepanyuk, P. Lang, R. Zeller, P. H. Dederichs, *Phys. Rev. Lett.* **75**, 509 (1995).
21. We note that the spin polarization shown here is not identical with the local magnetic moment of the sample because it is obtained at a certain energy.
22. O. O. Brovko, W. Hergert, V. S. Stepanyuk, *Phys. Rev. B* **79**, 205426 (2009).
23. D. M. Eigler, E. K. Schweizer, *Nature* **344**, 524 (1990).
24. H. C. Manoharan, C. P. Lutz, D. M. Eigler, *Nature* **403**, 512 (2000).
25. J. A. Stroscio, D. T. Pierce, A. Davies, R. J. Celotta, M. Weinert, *Phys. Rev. Lett.* **75**, 2960 (1995).

26. We thank F. Donati for enlightening discussions, N. Kurowsky for expert technical support, and O. O. Brovko for carefully reading this manuscript. Supported by Deutsche Forschungsgemeinschaft grant SFB 762.

Supporting Online Material

www.sciencemag.org/cgi/content/full/327/5967/843/DC1
Materials and Methods
SOM Text
Figs. S1 to S4
References

12 October 2009; accepted 11 December 2009
10.1126/science.1183224

Multiple Functional Groups of Varying Ratios in Metal-Organic Frameworks

Hexiang Deng, Christian J. Doonan, Hiroyasu Furukawa, Ricardo B. Ferreira, John Towne, Carolyn B. Knobler, Bo Wang, Omar M. Yaghi*

We show that metal-organic frameworks (MOFs) can incorporate a large number of different functionalities on linking groups in a way that mixes the linker, rather than forming separate domains. We made complex MOFs from 1,4-benzenedicarboxylate (denoted by "A" in this work) and its derivatives -NH_2, -Br, -$(Cl)_2$, -NO_2, -$(CH_3)_2$, -C_4H_4, -$(OC_3H_5)_2$, and -$(OC_7H_7)_2$ (denoted by "B" to "I," respectively) to synthesize 18 multivariate (MTV) MOF-5 type structures that contain up to eight distinct functionalities in one phase. The backbone (zinc oxide and phenylene units) of these structures is ordered, but the distribution of functional groups is disordered. The complex arrangements of several functional groups within the pores can lead to properties that are not simply linear sums of those of the pure components. For example, a member of this series, MTV-MOF-5-EHI, exhibits up to 400% better selectivity for carbon dioxide over carbon monoxide compared with its best same-link counterparts.

Crystalline extended structures are usually considered "simple" because they are constructed from a small number of distinct building units. Attempting to increase the number of such units in solids generally leads to either mixed phases, rather than a single phase of mixed units, or amorphous materials. In block copolymers, a minor modification to the side chains alters the entropy of the system and results in major (and often undesirable) changes in the structure of the polymer (*1*). Here, we show that by combining the inherent rigidity of metal-organic frameworks (MOFs) and the functional flexibility of polymers, one can overcome these challenges and create a large number of single-phase materials, each of which has multivariate (MTV) functionalities.

California Nanosystems Institute, University of California–Los Angeles (UCLA)–Department of Energy (DOE) Institute of Genomics and Proteomics, Department of Chemistry and Biochemistry, UCLA, 607 Charles E. Young Drive East, Los Angeles, CA 90095, USA.

*To whom correspondence should be addressed. E-mail: yaghi@chem.ucla.edu

Our strategy to making MTV-MOFs is to assemble their structures from links with different functional groups whose orientation, number, relative position, and ratio along the backbone (metal-oxide and phenylene units) can be controlled by virtue of the unchanged length of the link and its unaltered connectivity (Scheme 1). Such a construct can be viewed as having a primary structure composed of the simple repeating pattern of metal-oxide joints and organic links and a "complex" secondary structure formed by multivaried arrangements of many functional groups that are covalently bound to the links. In this way, each of the pores within the MOF would have an array of functionalities pointing into its center. Accordingly, the sequence of such functionalities and the frequency with which certain ones appear in the sequence will endow the pores with a new level of complexity that far exceeds any held by that of the original same-link MOFs—an aspect that may allow fine-tuning of the pore environment with favorable implications on properties.

Our past work (as well as the work of others) has shown that MOFs with two mixed links can be prepared, whereas a recent report showed that four different functionalities can be introduced into one structure by post-synthesis modification (*2*–*7*). These approaches are either confined to only two links or severely limited by having complete reactions at the links; multiple variations in link ratios and functionalities in these systems were not demonstrated. The present report describes a general method for producing crystalline MOF materials that combine sets of two to eight links of different functional groups; each set is incorporated into a single structure where the ratio of links is controlled, and the material can be produced with bulk purity. [Hereafter, A, 1,4-benzenedicarboxylate; B, -NH_2; C, -Br; D, -$(Cl)_2$; E, -NO_2; F, -$(CH_3)_2$; G, -C_4H_4; H, -$(OC_3H_5)_2$; and I, -$(OC_7H_7)_2$.] Specifically, we targeted the cubic MOF-5 structure (*8*) and combined the acid form of 1,4-benzenedicarboxylate (BDC), NH_2-BDC, Br-BDC, $(Cl)_2$-BDC, NO_2-BDC, $(CH_3)_2$-BDC, C_4H_4-BDC, $(OC_3H_5)_2$-BDC, and $(OC_7H_7)_2$-BDC links (Scheme 2, A to I, respectively) to form the corresponding sets of 18 MTV-MOFs, each having two or more different functionalities [two: MTV-MOF-5-AB, -AC, -AD, -AE, -AF, -AG, -AH, -AI, and -EI; three: MTV-MOF-5-ABC, -AHI, and -EHI; four: MTV-MOF-5-ABCD and -ACEF; five: MTV-MOF-5-ABCHI; six: MTV-MOF-5-ABCGHI; seven: MTV-MOF-5-ABCEGHI; eight: MTV-MOF-5-ABCEFGHI (Scheme 2)]. We describe their isolation as single phases, the structure of their MOF backbone, and their porosity, and show that this multivaried link synthetic strategy is useful for introducing functionalities [such as NO_2-BDC and $(Cl)_2$-BDC] into the MOF-5 type structure (MTV-MOF-5-AD and -AE) that do not form this structure when used alone. We also report our initial findings that members of this series (MTV-MOF-5-AHI and -EHI) show that the "whole is better than the sum of its parts," as evidenced by the fourfold enhancement of gas adsorption and separation properties of the multivaried